Earth and Planetary Science Letters 286 (2009) 171–183

Contents lists available at ScienceDirect

Earth and Planetary Science Letters

journal homepage: www.elsevier.com/locate/epsl

Seismic evidence for significant lateral variations in lithospheric thickness beneath the central and western North China Craton

Ling Chen *, Cheng Cheng, Zigen Wei

Seismological Laboratory (SKL-LE), Institute of Geology and Geophysics, Chinese Academy of Sciences, Beijing 100029, China

ARTICLE INFO

Article history:
Received 12 June 2009
Received in revised form 18 June 2009
Accepted 18 June 2009
Available online 14 July 2009

Editor: R.D. van der Hilst

Keywords:
North China Craton
lithospheric thickness
S-receiver functions
lithospheric thinning

ABSTRACT

We have migrated teleseismic S-receiver functions to construct detailed lithospheric structure images that cover the three constituent parts of the North China Craton (NCC). Our images show that in contrast to the eastern NCC where significantly thinned lithosphere (60–100 km) is widespread, the central and western NCC are characterized by the coexistence of both preserved thick and dramatically thinned lithosphere. The thick lithosphere (>200 km) is present beneath the stable Ordos Plateau and the thinned lithosphere (up to 80 km) is found in the late Cenozoic Yinchuan–Hetao and Shaanxi–Shanxi rift areas, with sharp changes occurring over a lateral distance of <200–400 km. Near the boundary between the eastern and central NCC, a rapid thickening of the lithosphere by 20–40 km over ~100 km laterally is observed, concordant with abrupt changes in surface topography and roughly coincident with the North–South Gravity Lineament (NSGL). Together with petrological and geochemical data these structural features suggest that lithospheric remobilization and thinning may have affected the NCC much further to the west than previously thought. Compared to the widespread reactivation and destruction of lithospheric mantle in the eastern NCC, lithospheric modification of the central and western NCC may have been less intensive and spatially more localized. Rifting and lithospheric reactivation probably occurred at mechanically weak boundary zones, but the cratonic nucleus of the Ordos block (which forms the western part of NCC) seems to have retained its rigidity, thickness, and stability over long periods of geological time. The long-term survival of such lateral contrasts suggests that the thick lithosphere is compositionally distinct from the convecting upper mantle.

1. Introduction

Cratons, formed mainly in the Archean era, are generally considered to be underlain by a thick, cold, and refractory mantle lithosphere and free from tectonic activity for billions of years. However, recent work suggests that cratons may not be as stable as previously thought. The cratonic lithosphere in some regions has been severely disturbed or reactivated, resulting in significant losses or modifications of the mantle root (e.g., Eggler et al., 1988; Menzies et al., 1993; Griffin et al., 1998; Brown et al., 1999; Lee et al., 2001). The North China Craton (NCC), the largest and oldest craton in China, is perhaps the most striking example of such reactivation (Carlson et al., 2005).

The NCC consists of three major parts (Fig. 1): the eastern NCC and the western NCC of Archean age, and the Trans-North China Orogen (the central NCC) which formed during the assembly of the eastern and western NCC ~1.85 Ga ago (Zhao et al., 2001). While the NCC was tectonically stable as a whole for more than 1 Ga and exhibited features similar to typical cratons ca 450 Ma ago (e.g., Menzies et al., 1993; Griffin et al., 1998; Gao et al., 2002), it experienced widespread thermotectonic reactivation in Phanerozoic time, with the three parts of the NCC evolving differently.

The eastern NCC was severely affected by this cratonic reactivation process. Abundant petrological and geochemical data (e.g., Menzies et al., 1993; Griffin et al., 1998; Fan et al., 2000; Xu, 2001; Wu et al., 2005; Menzies et al., 2007 and references therein) suggest that during the late Mesozoic, the eastern NCC was characterized by intensive lithospheric extension, high heat flow and voluminous magmatism. The thick cratonic lithosphere (>180 km) in this region lost a significant proportion of its deep mantle keel, accompanying a change in the nature of the lithosphere from cratonic to more fertile. Recent seismological investigations also have revealed a substantially thinned lithosphere on the order of 60–100 km and a well-marked lithosphere–asthenosphere boundary (LAB) beneath the eastern NCC (Zhu et al., 2002; Huang et al., 2003; Chen et al., 2006, 2008), which can be ascribed to the Mesozoic lithospheric reactivation of this region.

How the old lithosphere beneath the central and western NCC evolved in response to the late Mesozoic lithospheric reactivation or other tectonic events is still a matter of debate. Compared with the eastern NCC, these parts of the craton show little magmatic activity, relatively low heat flow (Wang et al., 1996; Hu et al., 2000) and generally thick crust (Ma, 1989; Li et al., 2006b) and lithosphere (Chen et al., 1991). Sharp changes in both surface topography and the gravity

* Corresponding author.
E-mail address: lchen@mail.iggcas.ac.cn (L. Chen).

0012-821X/$ – see front matter © 2009 Elsevier B.V. All rights reserved.
doi:10.1016/j.epsl.2009.06.022

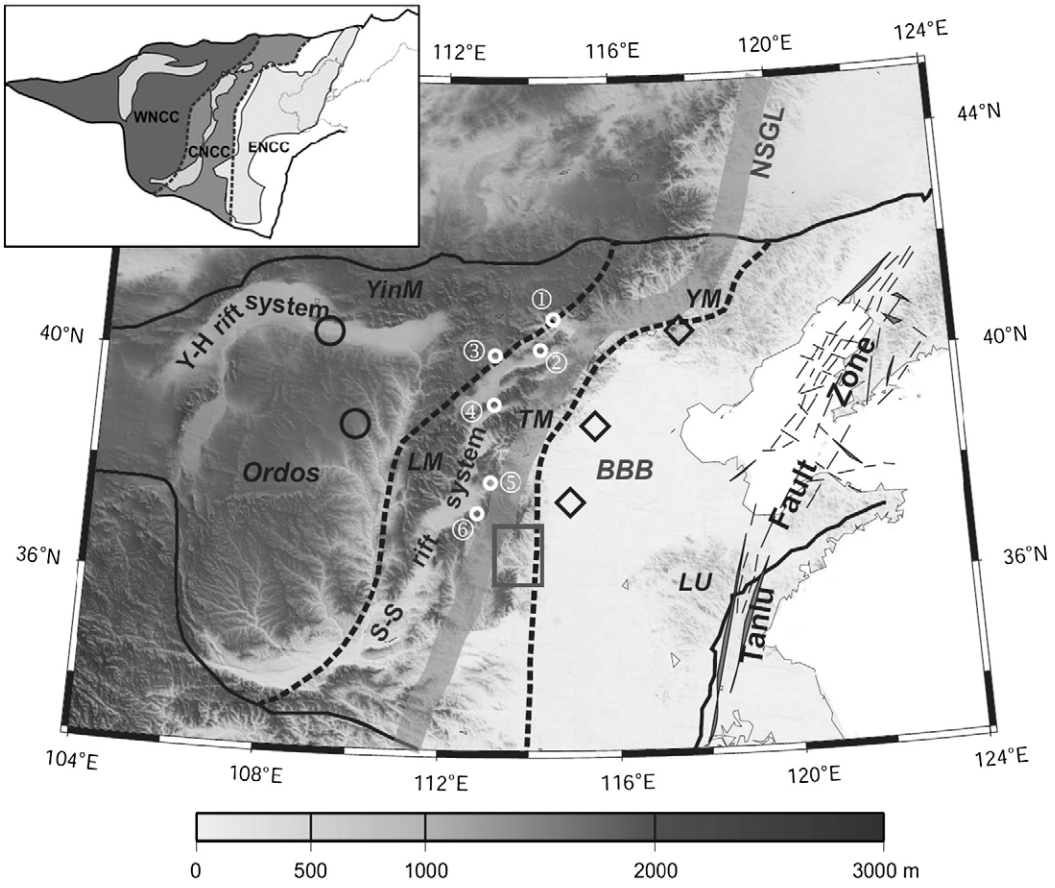

Fig. 1. Topographic map of the study region. Solid lines represent the boundary of the North China Craton (NCC), and two dashed lines outline the Trans-North China Orogen (the central NCC). White circles denote mantle xenolith localities (① Hannuoba; ② Yangyuan; ③ Datong; ④ Fanshi; ⑤ Xiyang–Pingding; ⑥ Zuoquan) and the gray rectangle shows Cretaceous intrusions under which lithospheric modification and thinning may have taken place as suggested by petrological and geochemical studies (e.g., Xu et al., 2004; Wang et al., 2006; Xu, 2007; Tang et al., 2008). Black circles mark places where the thickest (south, >200 km) and thinnest lithosphere (north, ~80 km) in the western NCC were imaged and diamonds show places where sharp changes in lithospheric thickness were observed near the boundary between the eastern and central NCC from S-receiver function (S-RF) migration (see Figs. 4 and 9). Thick gray line represents the North–South Gravity Lineament (NSGL). Major tectonic units in the NCC are also labeled, including the Tanlu Fault Zone, Luxi Uplift (LU), Bohai Bay Basin (BBB), Taihang Mountains (TM), Lüliang Mountains (LM), Yan Mountains (YM), Yin Mountains (YinM), Ordos Plateau, Yinchuan–Hetao (Y-H) and Shaanxi–Shanxi (S-S) rift systems. Map inset is a simplified geological map of the NCC showing the three-fold subdivision of the cratonic basement (Zhao et al., 2001) with Mesozoic–Cenozoic rift systems outlined in light gray.

field, as marked by the NNE-trending North–South Gravity Lineament (NSGL), roughly coincide with the boundary between the eastern and central NCC (Fig. 1). These observations have led to the idea that the central and western NCC have remained relatively stable and retained the characteristics of a typical craton.

However, recent petrological and geochemical studies (e.g., Xu et al., 2004; Wang et al., 2006; Xu, 2007; Tang et al., 2008) suggest that lithospheric remobilization and thinning may also have taken place around the rift areas or near the southeastern margin of the central NCC (see Fig. 1 for locations). In addition, lithosphere less than 100 km thick has been imaged along a NW–SE profile across the boundary between the eastern and central NCC (green line in Fig. 2, Chen, in press). Because of the paucity of data, however, the detailed lithospheric structural features beneath most of the central NCC and the western NCC, which are important for better understanding the tectonic evolution of the entire craton, have not been well understood.

In this study, we investigate the lithospheric structure of the three parts of the NCC by analyzing the new data collected at a dense broadband seismic station array in the western NCC and combining them with two previous data sets from stations in the eastern and central NCC (Fig. 2). We focus mainly on the lateral variations in the lithospheric thickness, particularly beneath the western and central NCC, and their correlations with the surface topography and the tectonic divisions of the region. We also discuss the implications of our observations for the destruction of the NCC's cratonic root.

2. Geological setting

The eastern NCC is dominated by lowlands with altitudes generally less than 200 m (Fig. 1). A large part of this region is covered by thick sedimentary basins including the Bohai Bay Basin in the north and the South North China Basin in the south. These basins are collectively called the North China rift system (light gray area within the eastern NCC in the map insert in Fig. 1) which has formed as a direct consequence of the widespread lithospheric extension during the late Mesozoic and early Cenozoic (Ren et al., 2002). The Tanlu Fault Zone, a large translithospheric strike-slip fault zone bounding the North China rift system to the east, developed during the collision between the NCC and the Yangtze Craton in the early Mesozoic (Yin and Nie, 1993; Zhang, 1997; Faure et al., 2001) and played an important role in the Mesozoic–Cenozoic lithospheric reactivation of the eastern NCC (Zheng et al., 1998; Xu, 2001; Xu et al., 2004). Highlands appear only locally in the eastern NCC, including the Luxi Uplift in the southeast, the eastern part of the Yan Mountains and the highland of Liaodong peninsula in the north and northeast. In contrast, the central and western NCC including the Taihang Mountains, Lüliang Mountains, the western part of the Yan Mountains, the Yin Mountains and the Ordos Plateau (Fig. 1) are characterized by high altitudes of >500 m, and up to 3500 m. Bordering the eastern NCC in the west and roughly coinciding with the NSGL, the Taihang Mountains formed as an extensional orogen in the late Mesozoic, the evolution of which has been tectonically coupled with

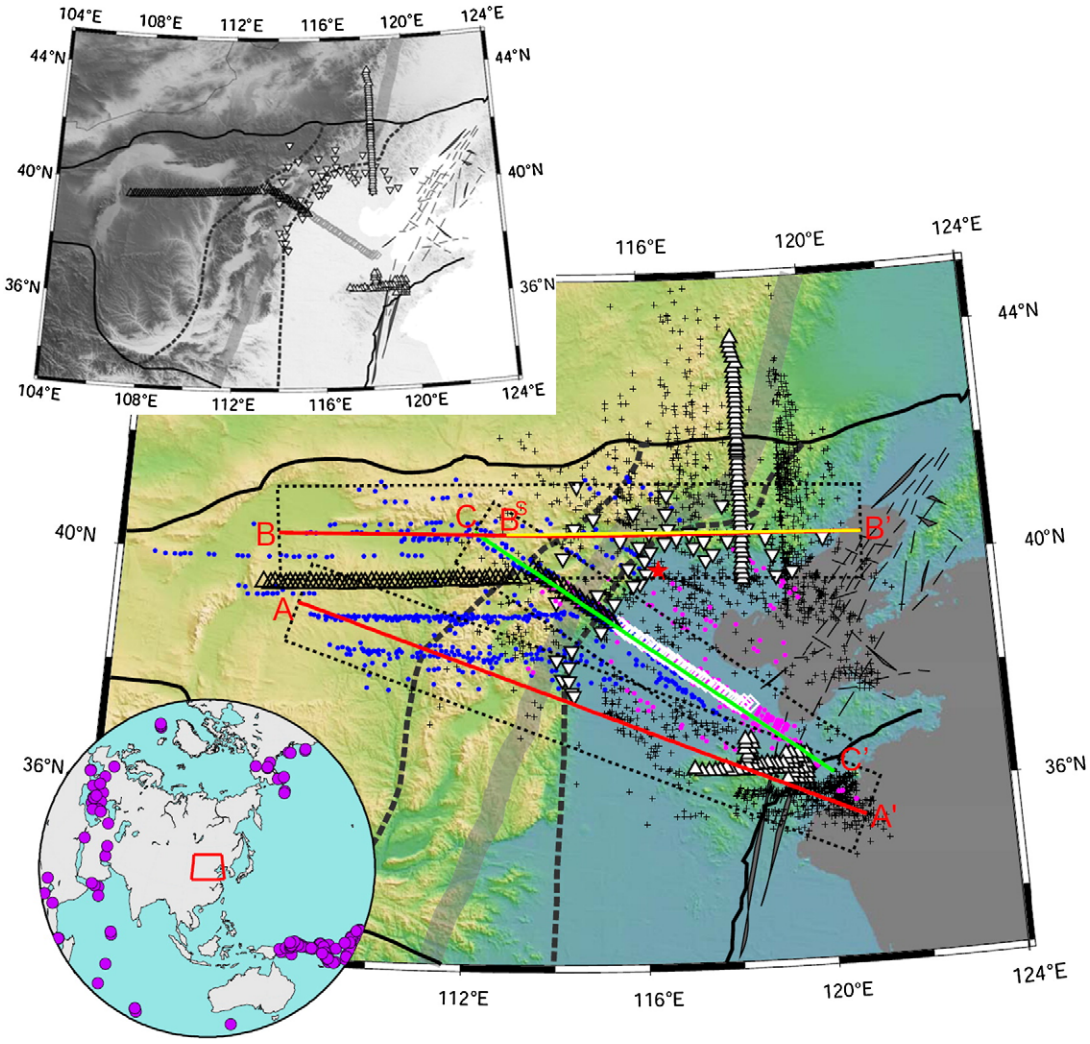

Fig. 2. Map of the study region. Solid red lines are the two profiles (A–A′ and B–B′) along which the lithospheric structural images were constructed in this study (Fig. 4) using S-RFs recorded at more than 200 broadband seismic stations (triangles and inverted triangles). Data from NCISP-I, III (solid triangles) and CEA stations (inverted triangles) have been used by Chen et al. (2008) in the study of regional lithospheric structure across the northeastern NCC, including profile B^S–B′ (in yellow). The NW–SE NCISP-II array, consisting of 20 stations located in the mountain region in the CNCC (open triangles) and 31 stations within the basin area in the ENCC (white diamonds, not considered in this study), were used by Chen (2009) to image the lithospheric structure along profile C–C′ (green line). The 50 NCISP-IV stations (open triangles) are located mostly within the WNCC and form a W–E linear array. The distribution of the stations is more clearly presented in the top inset. Piercing points at 100-km depth for S-to-P converted phases are shown as crosses (for stations used in Chen et al., 2008), purple dots (for basin stations) and blue dots (for stations marked by open triangles). The black rectangle around each profile marks the area where the S-RFs were projected onto the profile for imaging. Thick gray line represents the NSGL. Bottom inset shows the distribution of teleseismic events used. (For interpretation of the references to color in this figure legend, the reader is referred to the web version of this article.)

that of the Bohai Bay Basin to the east (Liu et al., 2000). On the other hand, the formation of the E–W trending Yin and Yan Mountains along the northern margin of the NCC (Fig. 1) was associated with several phases of N–S directed compressive deformation before the widespread late Mesozoic regional extension (Davis et al., 1998; Davis, 2003; Meng, 2003). The Ordos Plateau in the western NCC is a stable part of the craton with very low heat flow, little seismicity, and no internal deformation since the Precambrian (Zhai and Liu 2003; Kusky et al., 2007). In contrast to the eastern NCC, widespread lithospheric extension did not occur in the central and western NCC. Only two isolated rift systems developed surrounding the Ordos Plateau: the arc-shaped Yinchuan–Hetao rift to the northwest and the S-shaped Shaanxi–Shanxi rift to the east and southeast (Fig. 1) which represent the major tectonic features of the late Cenozoic extension in these regions (Zhang et al., 1998, 2003; Kusky et al., 2007).

3. S-RF images of the lithospheric structure

We used the S-receiver function (S-RF) technique to image the lithospheric structure of the NCC. The S-RFs contain information on S-to-P (Sp) conversions from deep velocity discontinuities, which can be used to constrain the depths of these discontinuities (Farra and Vinnik, 2000). Our study differs from previous S-RF studies for other regions (e.g., Li et al., 2004; Kumar et al., 2005; Li et al., 2007; Wittlinger and Farra, 2007) in that we applied a wave equation-based migration method to the S-RF data instead of the commonly used ray-theory-based stacking method. This migration method has already been proven to be more efficient than the stacking method in recovering complex structural features (Chen et al., 2005a,b) and has been successfully used in S-RF imaging of lithospheric structure in the northeastern NCC and around the eastern-central NCC boundary (Chen et al., 2008; Chen, 2009).

In this study, wave equation-based migration was performed on a combined S-RF data set collected from more than 200 broadband seismic stations in the NCC (Fig. 2). We incorporated 473 newly-constructed S-RFs from 50 NCISP-IV (a sub-project of NCISP, North China Interior Structure Project) broadband stations located in the western NCC with 382 S-RFs from 20 NCISP-II stations in the central NCC (a portion of the data set considered in Chen, 2009) and more than 2000 S-RFs (~1300 actually used in this study) from the NCISP-I,

III and CEA (China Earthquake Administration) stations mostly located in the eastern NCC (the data set of Chen et al., 2008). The NCISP-IV stations formed an E–W linear array near the northern boundary of the Ordos Plateau with inter-station spacing of ~10 km, and operated from September 2005 to September 2006 (Zhao et al., 2008). The detailed information about other stations can be found in Zheng et al. (2006), Chen et al. (2008) and at http://www.seislab.cn/data/. We applied a simplified method using a time-domain maximum entropy deconvolution of the vertical component by the radial to construct the S-RFs. Both synthetic modeling and applications to real data (Wittlinger et al., 2004; Chen et al., 2008; Chen, 2009) have suggested that this method is feasible for extracting the structural features of velocity discontinuities of various types, even under thick sedimentary basins. The resultant S-RFs were further band-pass filtered with corner frequencies of 0.03 Hz and 0.5 Hz to contain the same frequency contents as the S-RFs calculated before. The corresponding arrival times of Sp conversions relative to the direct S waves and piercing points of Sp conversions at depth were also calculated as we have done previously (Chen et al., 2008; Chen, in press). Following the migration procedure described by Chen et al. (2008), the S-RFs were processed with time-domain common conversion point (CCP) stacking and subsequent wave equation-based backward wavefield extrapolation to produce the lithospheric structure images along the two profiles A–A′ and B–B′ that traverse the three parts of the NCC (Fig. 2). The minimum S-RF number in each CCP stacking bin was set to 40 for the purpose of effective noise suppression. We adopted different frequency contents of the S-RFs in migration and also performed synthetic testing on the specifically designed models based on the actual data coverage. This allowed us to evaluate the robustness of the image features and to better constrain the lithospheric structure, especially the depth distribution of the LAB (see below).

Both the Moho and the LAB can be identified in the CCP stacked sections of the S-RFs (Fig. 3b and d), but they are more clearly seen in the migrated images (Fig. 4). While the Moho is only intermittently visible for profile A–A′ (Fig. 4a–c) due to the limited data coverage at shallow depths (Figs. 2 and 3a), it is continuous and smooth, and exhibits a gradual E–W deepening beneath profile B–B′ (Fig. 4d–f). The LAB, in contrast, is coherently detected along both profiles (Fig. 4). The generally similar appearances of the images from different frequency contents of data for each profile demonstrate the high reliability of our imaging results.

We identified the LAB Sp phase and estimated the LAB depths based on the following criteria: 1) The number of the S-RFs was sufficiently large (≥40) in each CCP stacking bin (see Fig. 3a and c); 2) The negative signal was clearly visible and could be traced continuously along the profile; 3) The signal was consistently imaged using different frequencies of the data; and 4) The image feature and depth of the signal agreed with synthetic modeling results or previous seismic observations if available.

We found that frequency analysis (3) and image comparisons (4) were highly necessary to reduce the uncertainties in the LAB depth estimation. For example, the LAB is clearly identified at ~80-km depth under the southeastern portion of profile A–A′ in the highest-frequency image (Fig. 4c). However, it cannot be determined without ambiguity near the northwestern end of the profile because of the presence of negative signals above 100 km, at ~170 km and below 200 km (Fig. 4c). With lower frequencies in migration, the signal at ~170-km depth becomes weaker and even invisible, and the deeper one appears smoother and more continuous (Fig. 4a and b). This indicates that the latter may represent a real structure, while the former probably reflects high-frequency scattering associated with small-scale heterogeneities in the upper mantle. In addition, our synthetic tests show that, under the current data conditions (Fig. 3a), a flattened segment of the LAB at ~170-km depth (dashed line in Fig. 5a) appears to be distorted similarly when different frequency ranges are considered

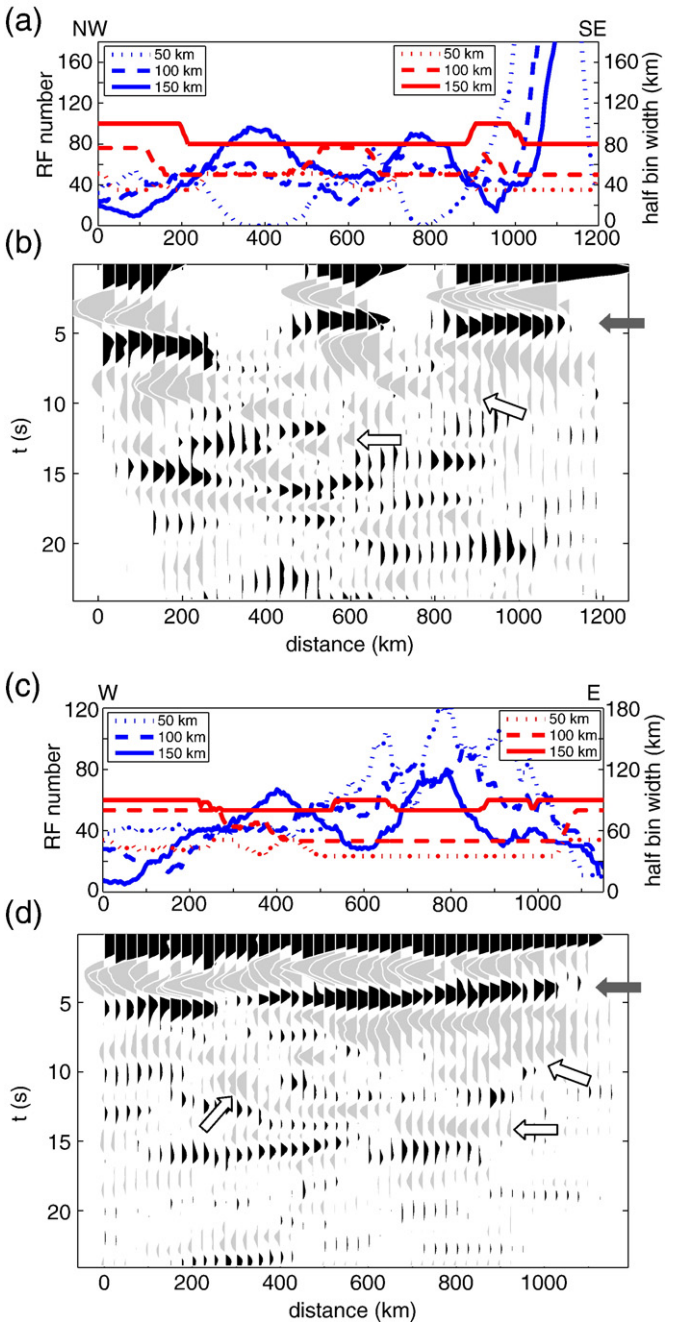

Fig. 3. Numbers of S-RFs in the CCP stacking bins (blue traces) and bin widths (red traces) and stacked sections of S-RFs (0.03–0.5 Hz) along profiles A–A′ (a, b) and B–B′ (c, d) after moveout corrected to the case of horizontal slowness $p=0$ (vertical incidence as required for migration, see Chen et al., 2005a, 2008). Time and amplitude axes are reversed, and positive amplitudes are plotted in black, negative amplitudes in gray. The Moho and LAB Sp conversion phases are marked by solid and open arrows, respectively. (For interpretation of the references to color in this figure legend, the reader is referred to the web version of this article.)

in migration (Fig. 5e–g). On the other hand, the synthetic images (Fig. 5b–d) for a continuously dipping LAB (thick solid line in Fig. 5a) resemble the data images (Fig. 4a–c) quite well. Synthetic modeling also suggests that the negative signals above 100-km depth around the northwestern end of the profile probably are Moho sidelobes or deconvolution artifacts (compare Fig. 5b–d with Fig. 4a–c). Even if the signals are real Ps phases, they may not result from the LAB because otherwise the strong and continuous deeper signal that can be observed in all the images at different

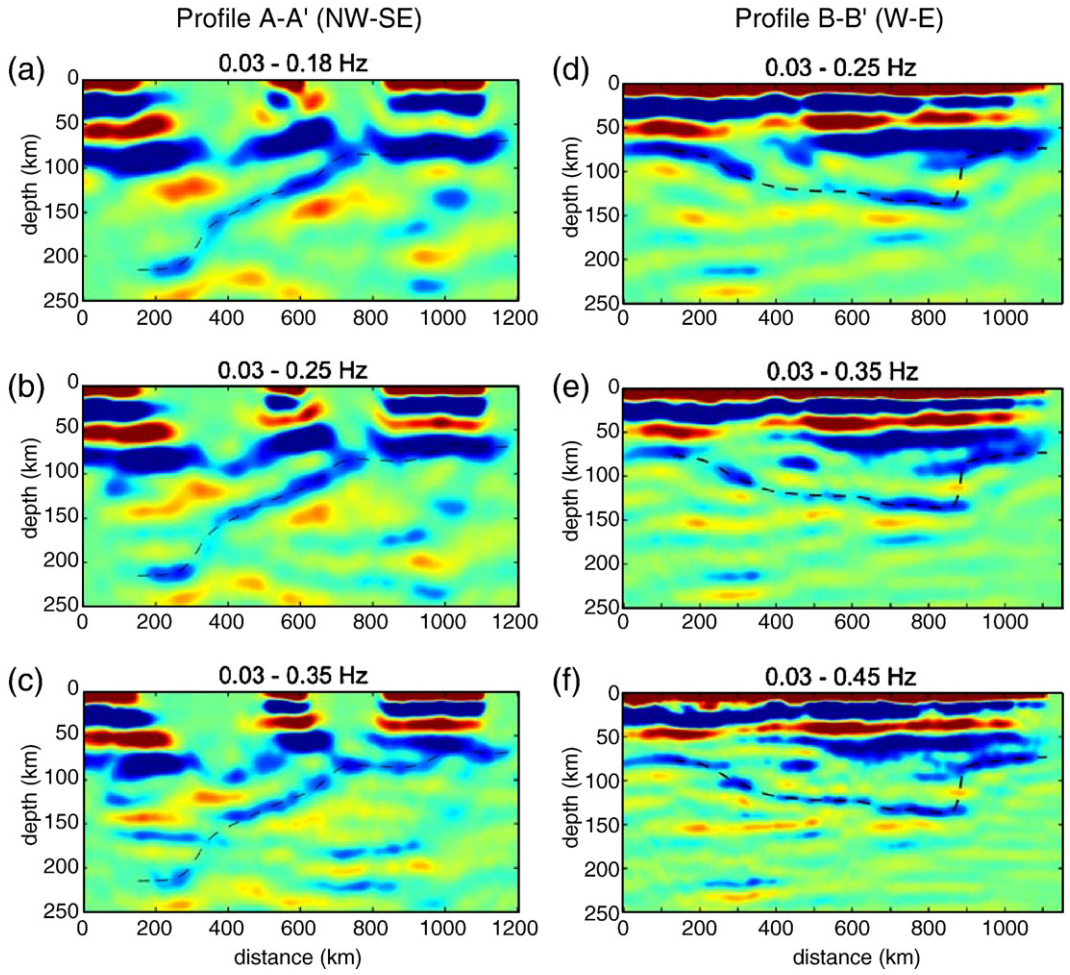

Fig. 4. Migrated S-RF images for profiles A–A′ (a–c) and B–B′ (d–f) using different frequency contents of data and adopting the average 1D velocity model for eastern NCC (Chen et al., 2006, 2008) in migration. Red and blue colors represent positive and negative amplitudes, respectively. Black dashed lines denote the LAB estimated from the highest-frequency images (c, f).

frequencies (Fig. 4a–c) would represent a strong discontinuity in the asthenosphere, which is physically unlikely. Moreover, this part of the profile is within the Ordos Plateau. A thicker lithosphere is consistent with the geological features and long-term tectonics of this area. From all these considerations, we therefore interpret the continuously dipping signal as the real LAB. With the shape of the LAB determined, we then estimated the LAB depths along profile A–A′ based on the highest-frequency image (Fig. 4c) because of its high resolution.

For profile B–B′, the LAB was detected more coherently when the highest-frequency data were incorporated in the migration (compare Fig. 4f with d and e). Therefore, the depths of the LAB were estimated directly from this image (Fig. 4f). We also compared our imaging result for profile B–B′ with that of a short profile (B^S–B′, yellow line in Fig. 2) previously obtained using a smaller set of data (Chen et al., 2008). Within the overlapping portion of the profiles the image features and the depth distributions of the LAB from the two studies agree well with each other, indicating the robustness of the revealed structural features (Fig. 6).

The LAB depths estimated in this way (black dashed lines in Fig. 4) show substantial lateral variations along the two profiles. With contributions mostly from the previous data set, the imaged LAB in the eastern parts of the profiles appears at similar depths as in previous images (compare Fig. 4 with Figs. 3d–f, 5 and 9 in Chen et al., 2008, also see Fig. 6c). It is significantly shallow, mostly in the depth range of 60–100 km in the eastern NCC (Fig. 4), and deepens abruptly by ~40-km near the boundary between the eastern and central NCC along profile B–B′ (Figs. 4d–f and 6). By incorporating the S-RF data from the dense NCISP-IV and NCISP-II seismic arrays (black open triangles in Fig. 2), it is possible to constrain the depth of the LAB in regions further to the west. Our imaging results reveal even more substantial undulations of the LAB in the central and western NCC. On the one hand, the LAB becomes gradually shallower along profile B–B′ from >130 km immediately to the west of the abrupt LAB step to ~80 km in the western NCC (Fig. 4d–f). On the other hand, the LAB dips monotonically from ~80 km near the boundary between the eastern and central NCC down to >160 km in the western part of the central NCC, and reaches depths of more than 200 km within the interior of the western NCC (Fig. 4a–c).

The significant lateral variations in the LAB depth imaged in this study cannot be induced by the use of an incorrect velocity model in the S-RF migration. By adopting different models including (1) an average 1-D crustal model for eastern China that we have used previously to image the lithospheric structure of the eastern NCC (Chen et al., 2006, 2008), or (2) 2-D models incorporating the lateral variations in crustal structure (e.g., Sun and Toksöz, 2006; Zheng et al., 2006; Sun et al., 2008) and uppermost mantle velocities of China (e.g., Pei et al., 2007), we obtained images similar to those shown in Fig. 4. The uncertainty in estimated LAB depth due to different models appears to be mostly less than 10 km, comparable to what can be resolved with the real S-RF data. This is analogous to the results of our previous studies (Chen et al., 2008; Chen, 2009) and also to those of other authors (e.g., Kumar et al., 2005; Li et al.,

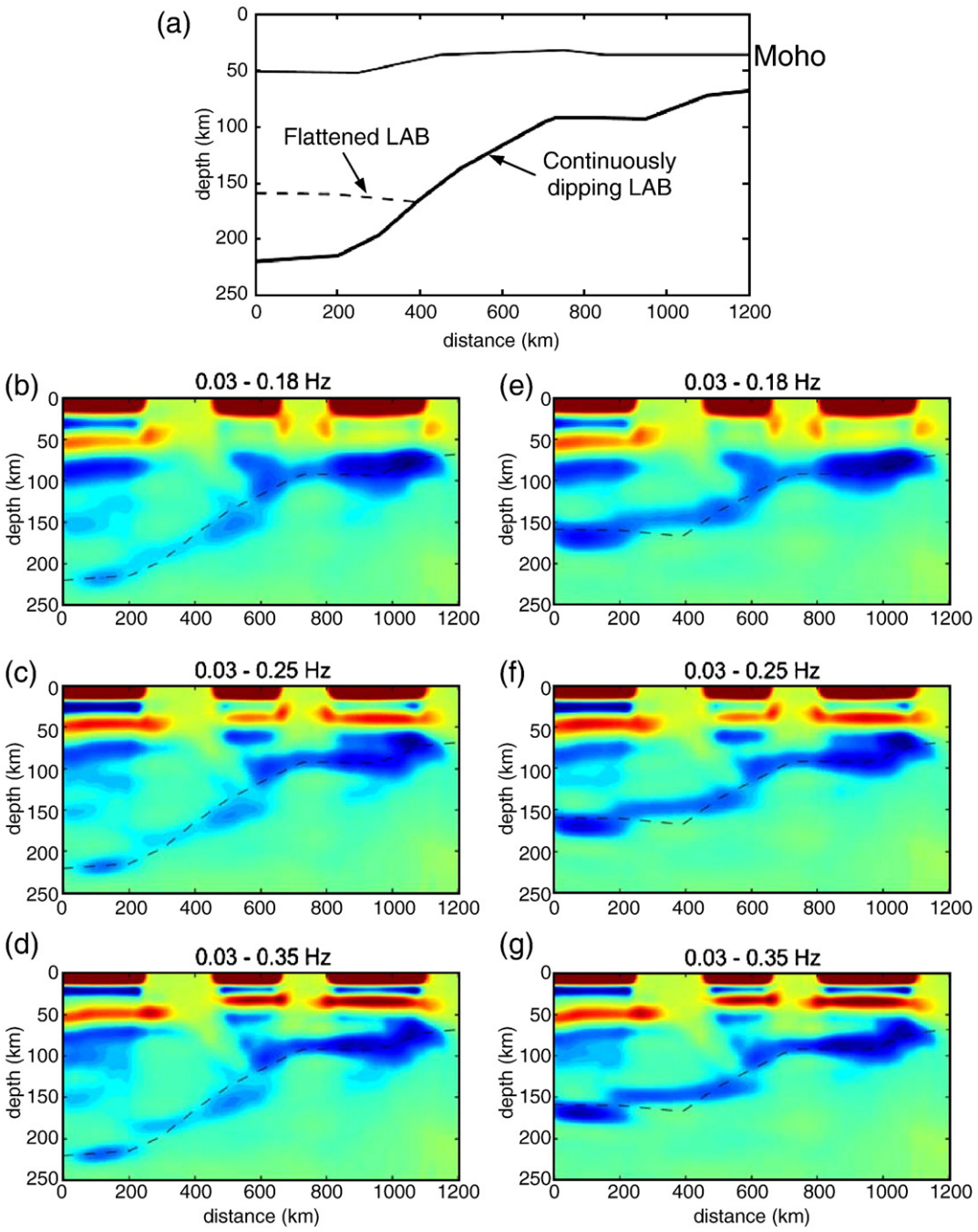

Fig. 5. Synthetic models (a) designed to simulate the structure observed in the real data image (Fig. 4c) for profile A–A′ and migrated S-RF images based on the real data distribution of profile A–A′ (Fig. 3a) for the models containing a continuously dipping LAB (b–d) and a flattened LAB at ~170-km depth (e–g). In both cases, a 20-km gradient zone with a 5% velocity drop for the LAB was used in the synthetic modeling. Dashed lines in (b–g) mark the LAB in each model.

2007). The imaged undulations of the LAB therefore appear to be required by the S-RF data.

4. Variations in lithospheric thickness beneath the western NCC

The most striking structural feature presented in our S-RF images is the substantial variation in the LAB depth from profile A–A′ to profile B–B′ in the northern part of the western NCC (Fig. 2). Specifically, the deep LAB of ~200 km along profile A–A′ appears beneath the stable Ordos Plateau, whereas the significantly shallower LAB of <100 km along profile B–B′ is within the Yinchuan–Hetao rift system immediately to the north. The deepest and shallowest LAB thus are imaged about 200 km distant from each other (black circles in Figs. 1 and 7a).

A rapid change in the lithospheric structure and the presence of significantly thinned lithosphere near the northern boundary of the western NCC was also suggested by a recent high-resolution surface-wave tomography study (Huang et al., 2008) which revealed a thick lithosphere (~160 km) under the Ordos Plateau and a thin lithosphere (~80 km) beneath the Yinshan Orogen (Fig. 7b). Note that the LAB depth beneath the Ordos was estimated to be ~160 km from surface-wave tomography (Huang et al., 2008), several tens of kilometers less than that derived here (>200 km). Considering the different sensitivities to the deep structure (surface waves reflect gradual variations, while S-RFs are sensitive to rapid changes in seismic velocity) and the

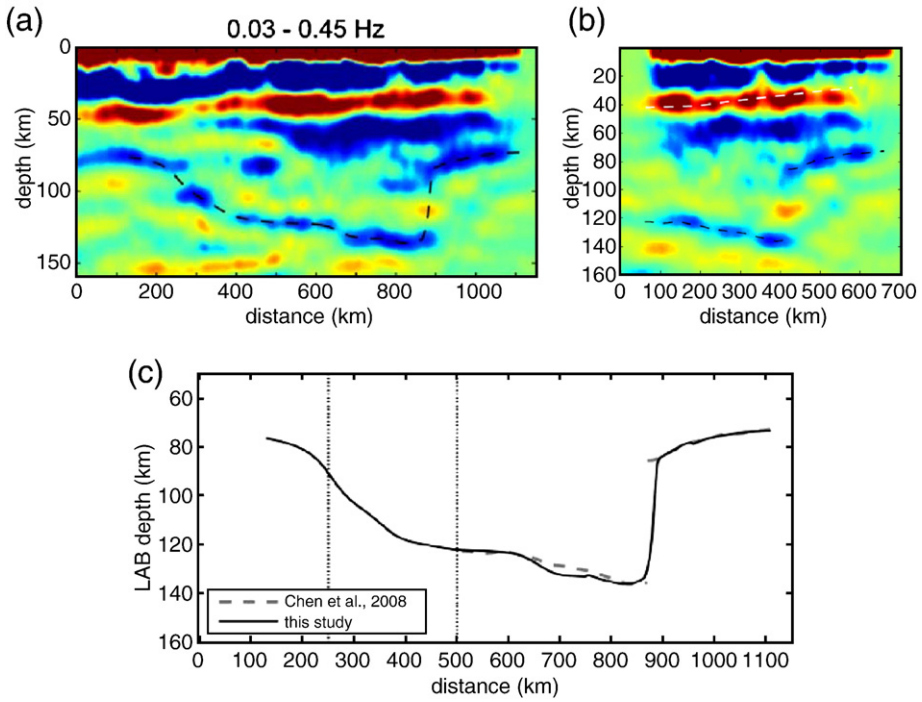

Fig. 6. Comparison between the S-RF image of profile B–B′ constructed in this study (a) (the upper part of Fig. 4f) and that of profile B^S–B′ with the same frequency contents (b) obtained by Chen et al. (2008) (Fig. 3f in Chen et al., 2008). See locations of the two profiles in Fig. 2. (c) Comparison of the estimated LAB depths from (a) and (b). Dotted lines mark the segment which has the same longitude range as the area immediately to the north of the NCISP-IV array (northern light blue rectangle in Fig. 7a) where a possible shallow LAB was suggested by P-RF imaging (Fig. 8f–i).

different lateral resolutions of the two sets of data (300~400 km for surface waves, Huang et al., 2008; and ~100 km for S-RFs, Chen et al., 2008; Chen, 2009), such a difference may not be significant, especially given the highly variable lithospheric structure in this region (e.g., Figs. 4 and 7b). We prefer a deeper LAB under the Ordos Plateau based on our S-RF images and P-RF analysis (see below) and a number of recent body wave tomography models which suggest a high velocity anomaly extending down to >200 km depth, even taking into account the relatively low depth resolution of such studies (e.g., Huang and Zhao, 2006; Li et al., 2006a; Tian et al., 2009).

The presence of a sharp structural change beneath this region was also hinted at by detailed P-RF analysis and imaging on the NCISP-IV data. The application of P-RFs in studying lithospheric structures is often hindered by the significant interference of crustal reverberations with P-to-S (Ps) phases from upper mantle discontinuities (e.g., Farra and Vinnik, 2000; Wittlinger and Farra, 2007; Chen et al., 2008; Chen, 2009). However, the higher the signal-to-noise ratios, the much larger number of P-RFs and the relatively high concentration of Ps piercing points at depth compared to Sp conversions (e.g., Fig. 7a) enable detailed analysis of the dependence of image features on azimuth, moveout correction scheme, and frequency contents of data. This is helpful in revealing short-wavelength structural heterogeneities beneath seismic arrays (e.g., Chen et al., 2006).

We analyzed a total of 3382 P-RFs collected at 48 NCISP-IV stations (the easternmost two stations in the Shanxi rift area were not considered because of the strong influence of thick sediments on P-RFs). These P-RFs were band-pass filtered with corner frequencies 0.03 Hz to 1 Hz and grouped into two subsets with non-overlapping back azimuth ranges: 90°–270° and −90°–90°, sampling the areas immediately south and north of the array, respectively (see the piercing point distribution in Fig. 7a). All the 1031 P-RFs in the northern group and either all 2351 P-RFs or a randomly selected subset of 1031 P-RFs in the southern group were processed individually in the subsequent wave equation migration. We did moveout corrections of the P-RFs based on the delay time variation of either Ps conversions (to enhance Ps phases) or PpPs multiples that arrive within the same time windows as Ps phases (to enhance multiple signals) in the CCP stacking, and then performed backward wavefield extrapolation on the stacked section using the migration velocities for Ps conversions (Chen et al., 2005a). Image comparison of the two moveout correction cases is helpful in distinguishing a real discontinuity structure from a multiple-induced artifact at a specific depth (e.g., Li et al., 2002; Chen et al., 2006).

Our migrated P-RF images show distinct structural features under the region (Fig. 8). The crustal images from the two groups of data appear similar, and the overall structure generally agrees with that derived by waveform inversion of all but higher-frequency P-RFs from the same array (Zheng et al., 2009). In particular, the two strong negative phases above the Moho, which may represent the upper interfaces of two low-velocity zones, and a depression of the Moho under the middle portion of the array (Fig. 8c,h) are all consistent with the crustal shear velocity model proposed by Zheng et al. (2009). However, substantial differences are observed at subMoho depths in the images from the two subsets of the data (Fig. 8), a situation that has not been reported previously. The image differences are present no matter which frequency contents of data were considered in the migration (compare Fig. 8a,b,f,g with 8c,d,h,i), and are independent of the number of data used. With the almost identical crustal images, the significantly different subMoho images cannot be explained by the influence of multiples produced at laterally varying intra-crust interfaces. Rather, these observations suggest that the structure below the Moho differs significantly from south to north across the NCISP-IV array.

To further understand the structural differences, we investigated in detail the dependence of the images on the moveout correction scheme. Except for the positive PpPs multiple of the Moho which is identified at ~160-km depth, all the images show strong negative signals at subMoho depths (Fig. 8a–d and f–i). For the southern area, most of these signals are enhanced by PpPs delay time-based moveout correction, and probably represent multiple phases from shallower structures (compared with synthetic modeling results in Fig. 8e). However, the signal at ~220 km depth in the western part of the

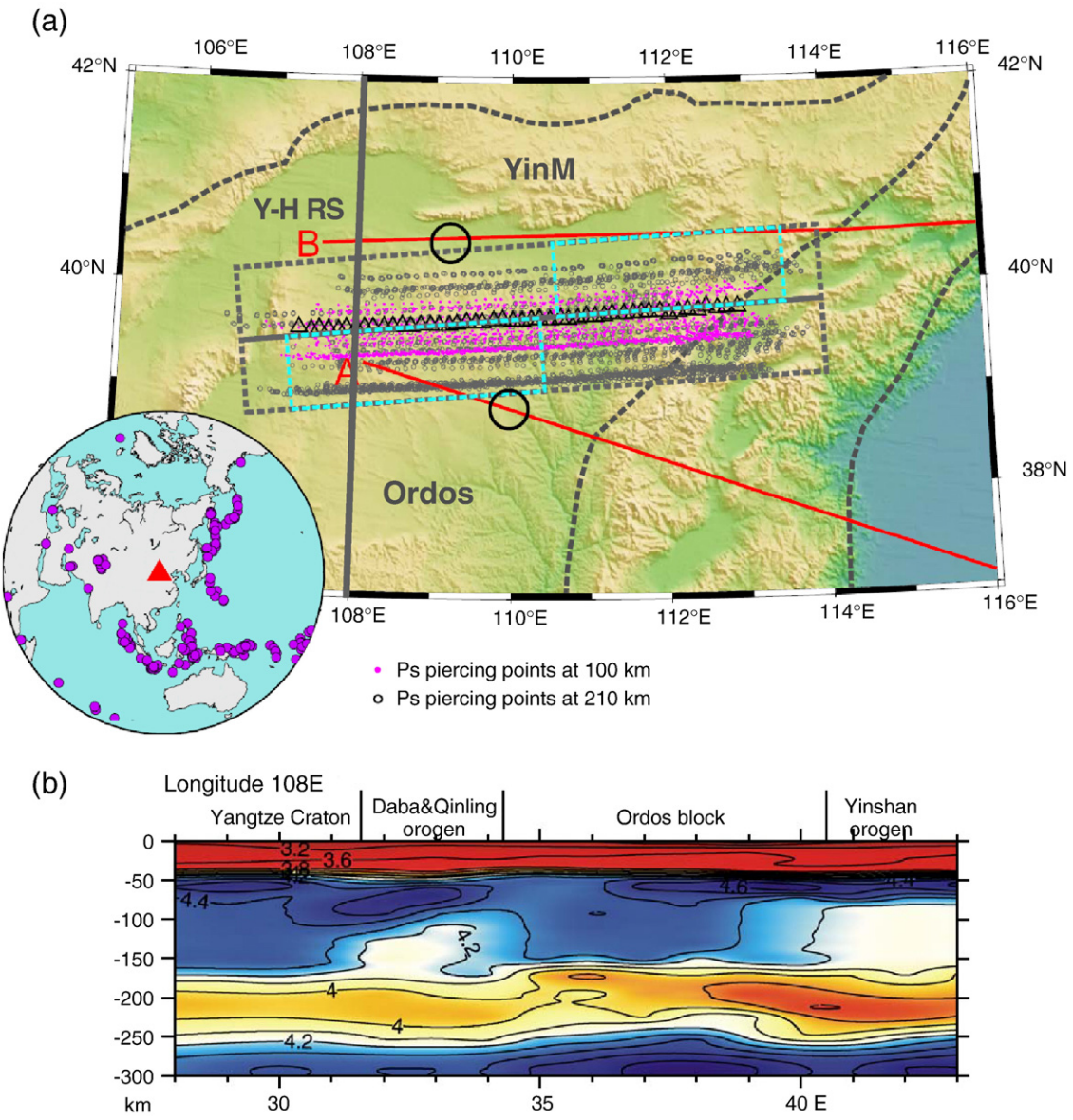

Fig. 7. (a) P-RF data coverage (Ps piercing point distributions) from the 48 NCISP-IV stations (black triangles) and blocks (gray rectangles) within which the corresponding data were migrated to construct the structural images (Fig. 8). Black circles mark the deepest and shallowest LAB imaged from the S-RFs along profiles A–A′ and B–B′ (red lines). Light blue rectangles represent the areas where possible Ps phases from the LAB may contribute to the respective P-RF images. Map inset shows the distribution of teleseismic events used for P-RF calculation. Y-H RS—Yinchuan–Hetao rift system, YinM—Yinshan Mountains. (b) surface-wave tomographic image along longitude 108°E (thick gray line in (a)) from Huang et al. (2008).

images exhibits contrastingly low amplitude ratios between the PpPs-based and Ps-based images (Fig. 8e and compare Fig. 8a,c with 8b,d). Considering the spatial coincidence of this signal with the deepest LAB (>200 km) imaged from the S-RFs (southern light blue block and black circle in Fig. 7a), a reasonable explanation is that the interaction between the real LAB Ps phase and the Moho PsPs + PpSs multiples results in the comparable amplitudes of the images (with a slightly larger one by Ps-based correction; Fig. 8e). The images for the northern area display different features and more complicated amplitude variations (Fig. 8f–i). Multiple negative signals are observed in the depth range from the Moho to the PpPs artifact (Fig. 8h–i). Some of them were enhanced by the PpPs-based moveout correction while others apparently were not (e.g., subMoho 1 and probably a part of subMoho 2). Low PpPs/Ps image ratios, probably reflecting real Ps conversions (Fig. 8j), were found at 80–120-km depth in the middle-to-eastern portion of the images (northeastern light blue block in Fig. 7a). This is also in accord with the S-RF image, which shows a shallower LAB rising westward from ~120 km to ~90 km at the same longitudinal locations along profile B–B′ (outlined in Fig. 6c).

The coincident N–S variations of both the P- and S-RF images as well as surface-wave tomographic images (compare Figs. 4, 7b, and 8) strongly suggest a sharp N–S change in the lithospheric structure near the NCISP-IV seismic array. The details of the structural change may be different from west to east, as indicated by the marked differences between the western and eastern parts of the P-RF images for both areas south and north of the array (Fig. 8). The LAB may be as deep as>200 km beneath the western part of the southern area, but there is little trace of a LAB phase under the eastern part (Fig. 8a–e). Comparisons between the P- and S-RF images (Figs. 6 and 8f–j) suggest that the LAB is probably shallow (<120 km) under the middle-to-eastern portion of the northern area. However, a strong negative signal appears at ~180–200-km depths under the western portion of the area (Fig. 8h and i). It was not enhanced by the PpPs-based moveout correction to a similar extent as the PpPs and PsPs + PpSs multiples of the Moho in both the data and synthetic cases (Fig. 8j),

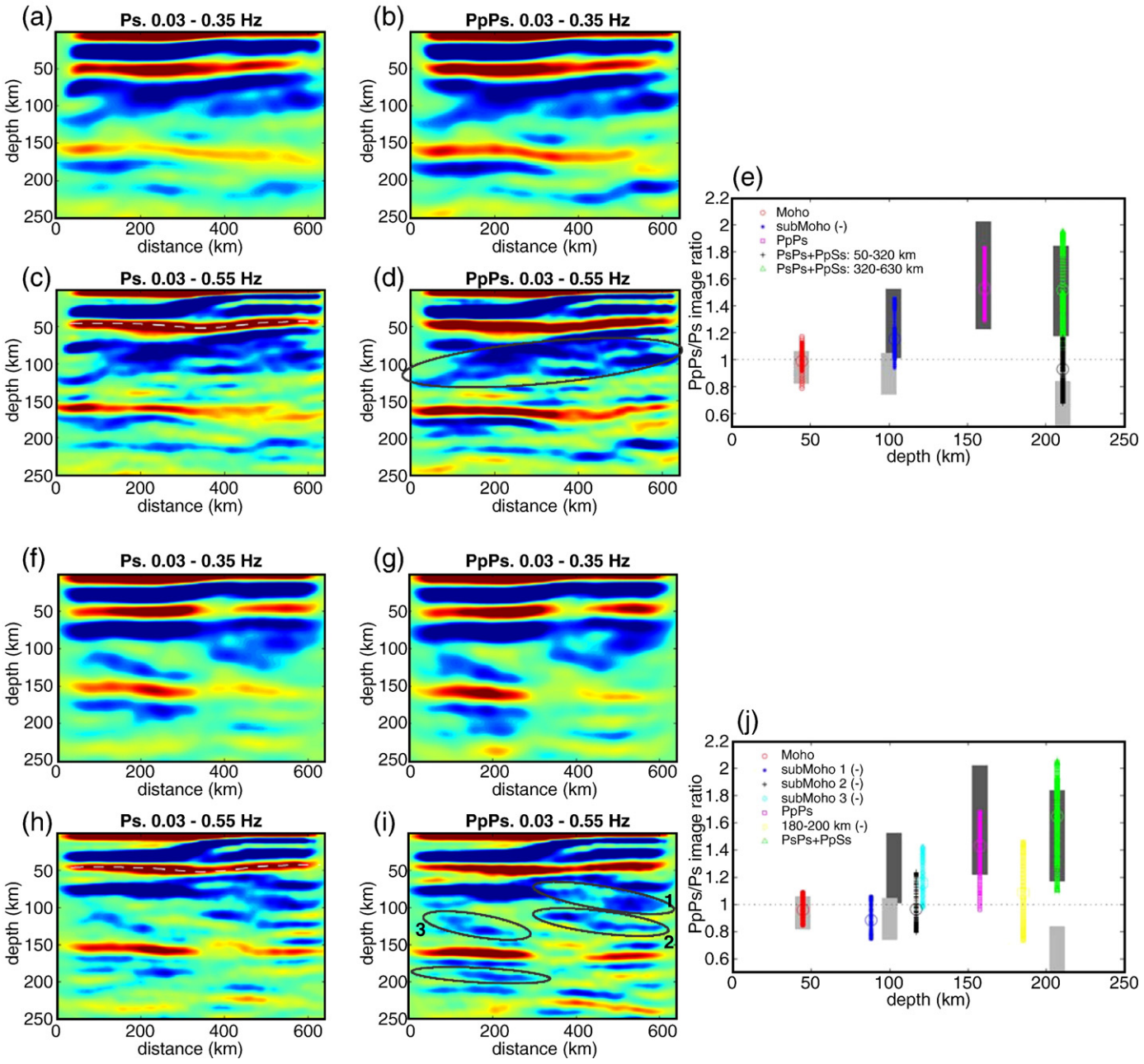

Fig. 8. Migrated P-RF images using the NCISP-IV data with back azimuths 90°–270° (a–d) and −90°–90° (f–i), respectively. The images were constructed with moveout corrections for either Ps (a, c, f, h) or PpPs phases (b, d, g, i) and with different frequency contributions of the data: (a, b, f, g) 0.03–0.35 Hz; (c, d, h, i): 0.03–0.55 Hz. (e, j) image ratios from (c, d) and (h, i), respectively, for signals at different depths. For clarity, some signals considered are marked by circles in (d) and (i). Shaded areas in (e, j) give the synthetic amplitude ratios for discontinuity structure images (light gray) and multiple-induced artificial images (dark gray) at the corresponding depths. White dashed lines in (c) and (h) denote the Moho estimated from the images.

indicating possible contributions from a real negative Ps phase, probably from the LAB. If this is further confirmed, these image features would suggest that a significant reduction in lithospheric thickness may occur further north in the west than in the east along the NCISP-IV array, and the structural change probably is much sharper near the shallowest LAB area imaged using the S-RFs (Fig. 7a). This actually corresponds well to the arcuate shape of the boundary between the Ordos and the Yinchuan–Hetao rift system as observed on the surface (Figs. 1 and 7a).

5. LAB depth vs. tectonic division (topography)

To gain further insight into the relationship between the lithospheric thickness and regional tectonics of all the constituent parts of the NCC, we compared the LAB depths derived from S-RF images with the altitudes and tectonic divisions along profiles A–A′, B–B′ and C–C′ (green line in Fig. 2); the lithospheric image of C–C′ was constructed by Chen (2009).

There is a general correlation between the LAB depth and surface topography (Fig. 9). For instance, shallower LAB (mostly <100 km) in the eastern NCC correlates well with lower altitudes (<500 m) in this region. Deeper LAB (>120 km) appears beneath the high mountains or plateaus in the central and western NCC (Fig. 9). The changes in both altitude and LAB depth are rather sharp along all the three profiles. The LAB deepens by 20–40 km over a lateral distance of ~100 km (marked by circles in Fig. 9a–c on the LAB depth plots), typically 50–100 km east of the boundary between the eastern and central NCC and 100–200 km east of the NSGL (Figs. 1 and 9). It was suggested

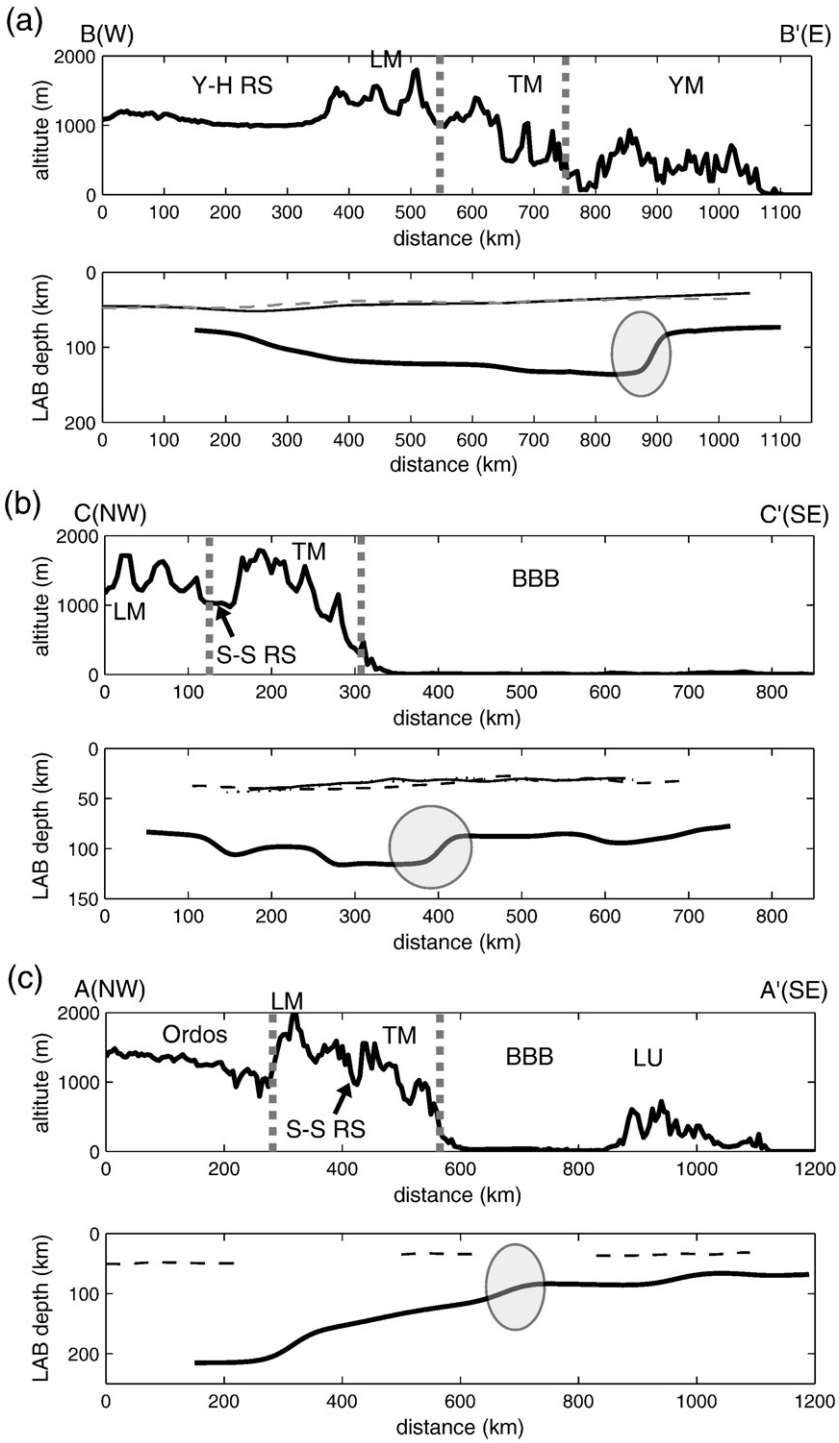

Fig. 9. Comparisons of the LAB depths with altitude and tectonic divisions along the three profiles B–B′ (a), C–C′ (b) (modified from Chen, in press), and A–A′ (c), from north to south. Circular areas mark the sharp changes in the LAB depth along the profiles. The widths of the circles represent the uncertainties on the transverse locations of the sharp changes, given the ~100-km lateral resolution that the S-RF imaging can achieve with the frequency range considered (Chen et al., 2008; Chen, 2009). Moho depths are also plotted for all the profiles with dashed lines denoting the Moho estimated from the migrated S-RF images and thin solid lines from P-RF imaging (A–A′: this study; B–B′: this study combined with Chen et al., 2008; C–C′: from Fig. 9 in Chen, 2009). Thick dotted gray lines represent the boundaries between the eastern, central, and western NCC. Y-H RS—Yinchuan–Hetao rift system; S-S RS—Shaanxi–Shanxi rift system. Abbreviations for other tectonic units are the same as those in Fig. 1.

previously that the NSGL represents a deep intra-continental boundary separating the NCC into topographically and tectonically different lithospheric domains (Griffin et al., 1998; Menzies and Xu, 1998; Zheng et al., 2006; Xu, 2007). Considering the ~100-km lateral resolution that the S-RF data can achieve (Chen et al., 2008; Chen, 2009), the 100–200 km discrepancy between the locations of the lithospheric thickness changes and the NGSL suggest that an intra-continental boundary, if it does exist and coincide with the NSGL on the surface, probably dips to the east at depth.

The deepest LAB of >200 km under the Ordos plateau (Fig. 9c) is consistent with recent tomographic imaging results (Huang and Zhao, 2006; Li et al., 2006a; Tian et al., 2009). The significantly shallower

LAB in the central and western NCC corresponds well to the location of the two rift systems (Fig. 9a and b): the Yinchuan–Hetao rift system in the western NCC (profile B–B′) and the Shaanxi–Shanxi rift system mostly in the central NCC (profile C–C′). However, no obvious uplift of the LAB appears across the Shaanxi–Shanxi rift system along profile A–A′ (Fig. 9c). The surface expression of the rift is much narrower (Fig. 9c) compared with that in the other two profiles (Fig. 9b and c). Under this rift area, probably either the LAB is deep or the uplift of the LAB is too localized to be detected seismologically.

6. Discussion and conclusions

Our S-RF imaging results reveal that, besides the widespread thinned lithosphere in the eastern NCC, reported previously based on seismological (Chen et al., 1991; Zhu et al., 2002; Huang et al., 2003; Chen et al., 2006, 2008) as well as geochemical, geothermal and petrographic observations (Griffin et al., 1998; Fan et al., 2000; Xu, 2001; Menzies et al., 2007), a shallow LAB is also present in the central and western NCC, mainly confined to the rift areas (Figs. 4 and 9). Compared to the eastern NCC, the lithospheric thickness in the central and western NCC is even more variable, ranging from around 80 km to more than 200 km, suggesting the coexistence of both thinned and preserved thick lithosphere and marked structural heterogeneities in these regions.

The variation of lithospheric thickness in the western and central NCC is not only large but also sharp, especially between the Ordos Plateau and the surrounding rift areas. Our migrated S-RF images show a thickness reduction of more than 100 km occurring over a lateral distance of ~200 km from the Ordos Plateau in the south to the Yinchuan–Hetao rift system in the north (circles in Figs. 1 and 7a). The lithospheric structural change in this region probably is even sharper locally and differs from east to west, as suggested by detailed P-RF analysis and imaging results (Fig. 8), and appears to be correlated with surface geology (Figs. 1 and 7a). The difference in lithospheric thickness between the Ordos and the Shaanxi–Shanxi rift system is comparable in magnitude, though over a larger distance (300–400 km).

Such short-wavelength structural variations may reflect different lithospheric properties and/or tectonic processes of the region. Lying between the Ordos Plateau and the Yin Mountains near the northwestern boundary of the NCC (Fig. 1), the Yinchuan–Hetao rift system may be an ancient mechanically weak zone. The localization of this Cenozoic rift system may have been affected by several tectonic processes, such as the multiple Mesozoic compression events that induced the development of the Yin and Yan Mountains (Davis et al., 1998; Davis, 2003; Meng, 2003) and the earlier accretional tectonics in the Central Asia Orogenic Belt immediately to the north (Wang and Mo, 1995; Zorin, 1999; Windley et al., 2007 and references therein). The Shaanxi–Shanxi rift system is within the central NCC and close to the boundary between the western and central NCC (Fig. 1). It may also have been mechanically weak ever since the formation of the central NCC during the amalgamation of the eastern and western NCC in Paleoproterozoic time. Indeed, preexisting weak zones/structures in the lithosphere are expected to be susceptible to magmatic activity and tectonic deformation, and therefore can function as the primary control on the tectono-thermal evolution of continental regions (Bell et al., 2003; Savage and Silver, 2008; Begg et al., 2009).

It is possible that during the long-term evolution of the NCC successive tectonic events have repeatedly influenced the boundary areas around the Ordos Plateau. Lithospheric extension and thinning may have been preferentially initiated and intensified along these weak zones, eventually leading to rifting. In contrast, the Archean Ordos Plateau seems to have been less affected tectonically, and the cratonic nucleus of the region probably has remained rigid and stable against tectonic deformation for thousands of Ma. These differences in lithosphere properties and tectonics may account for the sharp change between the preserved thick mantle root beneath the Ordos and the significantly thinned lithosphere under the surrounding rift systems at the present time.

This marked change in lithospheric structure is not a unique feature of the NCC. Comparable and even sharper structural changes have been reported in some other continental regions, especially near the boundaries of cratons. For example, the Sorgenfrei–Tornquist Zone, which separates the accretionary mobile belts in the central European platform and the Precambrian eastern European craton to the east and north-east, is characterized by a step-like increase of ca 150 km in lithospheric thickness over a lateral distance of 100 km (e.g., Zielhuis and Nolet, 1994; Shomali et al., 2006). Sharp variations in lithospheric structure are also found in the Baikal rift area around the southern boundary of the Siberian craton (Lebedev et al., 2006) and the boundary zones between tectonic blocks of different ages (including Archean) in continental Australia (Zielhuis and van der Hilst, 1996; Simons et al., 1999; Fishwick et al., 2008). Numerical simulations suggest that large thermal and composional differences, and thus a distinct rheological contrast between the two sides, may be responsible for the preservation of such sharp lithospheric structural changes against thermo-mechanical erosion by active mantle convection for hundreds of Ma (Hieronymus et al., 2007). A change in the lithospheric properties therefore may also explain the observed sharp variations in lithospheric structure at the boundary areas in the western and central NCC and in other cratonic boundary regions mentioned above.

The different structural features of the present-day lithosphere between the eastern NCC and the central and western NCC and particularly the distinct changes in the lithospheric thickness near the boundary between these two domains (Figs. 4 and 9, Fig. 9 in Chen et al., 2008) may reflect different tectonic processes on the opposite sides of the NSGL, especially during the Phanerozoic. The widespread thinned lithosphere to the east, in contrast to the typical cratonic lithosphere >180 km thick, attests that the lithosphere of the eastern NCC has been largely modified or destroyed probably mostly during the late Mesozoic reactivation process. The thinned crust (<35 km; Fig. 9, Li et al., 2006b; Zheng et al., 2006) and active seismicity (Gu, 1983; Kusky et al., 2007) further suggest that the craton destruction in this region may not only have been widespread laterally but also have involved the entire lithosphere vertically. Modeling studies of lithospheric stability suggest that, because of the minimal effects of thermo-mechanical erosion by mantle convection, cratonic lithosphere cannot be thinned significantly over a timescale much shorter than 2 Ga (Lenardic and Moresi, 1999; King, 2005; Hieronymus et al., 2007). The fundamental destruction of the eastern NCC therefore would require processes other than mantle convection of stable patterns (e.g., induced by LAB topography), probably either chemical erosion (including mantle–melt interaction) in conjunction with thermo-mechanical erosion (e.g., Xu, 2001; Zhang, 2005) and/or "top-down" lithospheric delamination induced by gravitational instability (e.g., Wu et al., 2003; Gao et al., 2004).

In contrast to the eastern NCC, a thinned lithosphere is only observed locally under the two rift areas in the central and western NCC, and a thick lithospheric mantle root extends to ~200 km depth underneath the Ordos Plateau. These observations, together with a thicker crust (~40–50 km in general and >37 km even beneath rift zones; Fig. 9, Li et al., 2006b; Chen, 2009; Zheng et al., 2009) makes it unlikely that the Phanerozoic lithospheric reactivation has significantly affected regions west of the NSGL. Lithospheric modification processes may have already impacted on the structure and/or nature of the lithosphere under the Shaanxi–Shanxi rift system, as indicated by the thinned lithosphere (Fig. 9b), isotopic and chemical heterogeneities of mantle xenoliths (Xu et al., 2004; Xu, 2007; Tang et al., 2008), and numerous earthquakes (Liu et al., 2007). Although mantle xenolith data are lacking, this may also be true for the Yinchuan–Hetao rift system, given its (even more) strongly thinned lithosphere and similar Cenozoic tectonics and seismicity. The presence of thick lithosphere under the Ordos Plateau (Figs. 4a–c, 7b, 9c)

corresponds to the well stratified crustal structure of Precambrian shield type (Zheng et al., 2009) and the lack of earthquakes in this region. All these features suggest that the lithospheric modification may either have not been processed to reach the high-viscosity core of cratonic nucleus in the western NCC or probably is too weak to be detected seismologically, even taking into account the effects of convective erosion from the underlying mantle.

Our migrated S- and P-RF images constructed using dense seismic array data have revealed substantial variations in lithospheric thickness across the NCC that appear to be closely correlated with surface topography and the tectonic divisions of the region. A better understanding of the correlation between the crustal tectonics, lithospheric processes and deep mantle dynamics of the NCC demands systematic comparisons of the crustal, lithospheric and deep mantle structures and deformation patterns among different parts of the craton. This is beyond the scope of this paper and will be addressed in detail elsewhere.

Acknowledgments

We sincerely thank the participants of the Seismic Array Laboratory in the Institute of Geology and Geophysics, Chinese Academy of Sciences and the China Earthquake Administration for providing the waveform data. We also wish to thank Zhongxian Huang for providing the surface-wave tomographic image, Fuyuan Wu and Yigang Xu for thoughtful discussions, and Bill Griffin for comments and proof-reading. We are grateful to Editor Robert D. van der Hilst and two anonymous reviewers for their constructive comments and suggestions, which significantly improved the manuscript. This research is supported by the National Science Foundation of China (Grants 90814002 and 40674029) and Chinese Academy of Sciences.

References

Begg, G.C., Griffin, W.L., Natapov, L.M., O'Reilly, SuzanneY., Grand, S.P., O'Neill, C.J., et al., 2009. The lithospheric architecture of Africa: seismic tomography, mantle petrology, and tectonic evolution. Geosphere 5, 23–50.

Bell, D.R., Schmitz, M.D., Janney, P.E., 2003. Mesozoic thermal evolution of the southern African mantle lithosphere. Lithos 71, 273–287.

Brown, R.W., Gallagher, K., Griffin, W.L., et al., 1999. Kimberlites, accelerated erosion and evolution of the lithospheric mantle beneath the Kaapvaal craton during the mid-Cretaceous. Ext. Abst., 7th Int. Kimb. Conf. pp. 105-107.

Carlson, R.W., Pearson, D.G., James, D.E., 2005. Physical, chemical, and chronological characteristics of continental mantle. Rev. Geophys. 43 2004RG000156.

Chen, L., 2009. Lithospheric Structure variations between the eastern and central North China Craton from S- and P-receiver function migration. Phys. Earth Planet. Inter. 173, 216–227.

Chen, G.Y., Song, Z.H., An, C.Q., et al., 1991. Three dimensional crust and upper mantle structure of the North China region. Acta Geophys. Sinica 34, 172–181 (in Chinese with English abstract).

Chen, L., Wen, L.X., Zheng, T., 2005a. A wave equation migration method for receiver function imaging, (I) theory. J. Geophys. Res. 110, B11309. doi:10.1029/2005JB003665.

Chen, L., Wen, L.X., Zheng, T., 2005b. A wave equation migration method for receiver function imaging, (II) application to the Japan subduction zone. J. Geophys. Res. 110, B11310. doi:10.1029/2005JB003666.

Chen, L., Zheng, T.Y., Xu, W.W., 2006. A thinned lithospheric image of the Tanlu Fault Zone, eastern China: constructed from wave equation based receiver function migration. J. Geophys. Res. 111, B09312. doi:10.1029/2005JB003974.

Chen, L., Wang, T., Zhao, L., Zheng, T.Y., 2008. Distinct lateral variation of lithospheric thickness in the Northeastern North China Craton. Earth Planet. Sci. Lett. 267, 56–68.

Davis, G.A., 2003. The Yanshan Belt of North China: tectonics, adakitic magmatism, and crustal evolution. Earth Sci. Frontiers 10, 373–384.

Davis, G.A., Wang, C., Zheng, Y., et al., 1998. The enigmatic Yinshan fold-and-thrust belt of northern China: new views on its intraplate contractional styles. Geology 26, 43–46.

Eggler, D.H., Meen, J.K., Welt, R., et al., 1988. Tectonomagmatism of the Wyoming Province. Colo. Sch. Mines Q. 83, 25–40.

Fan, W.M., Zhang, H.F., Baker, J., Jarvis, K.E., Mason, P.R.D., Menzies, M.A., 2000. On and off the North China Craton: where is the Archaean keel? J. Petrol. 41, 933–950.

Faure, M., Lin, W., Breton, N.L., 2001. Where is the North China–South China block boundary in eastern China? Geology 29, 119–122.

Farra, V., Vinnik, L., 2000. Upper mantle stratification by P and S receiver functions. Geophys. J. Int. 141, 699–712.

Fishwick, S., Heintz, M., Kennett, B.L.N., Reading, A.M., Yoshizawa, K., 2008. Steps in lithospheric thickness within eastern Australia, evidence from surface wave tomography. Tectonics 27, TC4009. doi:10.1029/2007TC002116.

Gao, S., Rudnick, R.L., Carlson, R.W., McDonough, W.F., Liu, Y.S., 2002. Re–Os evidence for replacement of ancient mantle lithosphere beneath the North China Craton. Earth Planet. Sci. Lett. 198, 307–322.

Gao, S., Rudnick, R.L., Yuan, H.L., 2004. Recycling lower continental crust in the North China craton. Nature 432, 892–897.

Griffin, W.L., Zhang, A.D., O'Reilly, S.Y., Ryan, G., 1998. Phanerozoic evolution of the lithosphere beneath the Sino-Korean Craton. In: Flower, M., Chung, S.L., Lo, C.H., Lee, T.Y. (Eds.), Mantle dynamics and plate interactions in East Asia: Am. Geophys. Union Geodyn. Ser., vol. 27, pp. 107–126.

Gu, G., 1983. Catalogue of Chinese Earthquakes (1831 BC–1980 AD). Science Press, Beijing. (in Chinese).

Hieronymus, C.F., Shomali, Z.H., Pedersen, L.B., 2007. A dynamical model for generating sharp seismic velocity contrasts underneath continents: application to the Sorgenfrei–Tornquist Zone. Earth Planet. Sci. Lett. 262, 77–91.

Hu, S., He, L., Wang, J., 2000. Heat flow in the continental area of China: a new data set. Earth Planet. Sci. Lett. 179, 407–419.

Huang, Z., Su, W., Peng, Y., Zheng, Y., Li, H., 2003. Rayleigh wave tomography of China and adjacent regions. J. Geophys. Res. 108 (B2), 2073. doi:10.1029/2001JB001696.

Huang, J., Zhao, D., 2006. High-resolution mantle tomography of China and surrounding regions. J. Geophys. Res. 111, B09305. doi:10.1029/2005JB004066.

Huang, Z., Li, H., and Zheng, Y., 2008. The lithosphere of North China Craton from surface wave tomography. Earth Planet. Sci. Lett., revision submitted.

King, S.D., 2005. Archean cratons and mantle dynamics. Earth Planet. Sci. Lett. 234, 1–14.

Kusky, T.M., Windley, B.F., Zhai, M.-G., 2007. Tectonic evolution of the North China Block: from orogen to craton to orogen. Geological Society, London, Special Publications, vol. 280, pp. 1–34.

Kumar, P., Kind, R., Hanka, W., et al., 2005. The lithosphere–asthenosphere boundary in the North–West Atlantic region. Earth Planet. Sci. Lett. 236, 249–257.

Lee, C.-T.A., Yin, Q., Rudnick, R.L., et al., 2001. Preservation of ancient and fertile lithospheric mantle beneath the southwestern United States. Nature 411, 69–73.

Lebedev, S., Meier, T., van der Hilst, R.D., 2006. Asthenospheric flow and origin of volcanism in the Baikal Rift area. Earth Planet. Sci. Lett. 249, 415–424.

Lenardic, A., Moresi, L.-N., 1999. Some thoughts on the stability of cratonic lithosphere: effects of buoyancy and viscosity. J. Geophys. Res. 104, 12747–12758.

Li, A., Fischer, K.M., van der Lee, S., Wysession, M.E., 2002. Crust and upper mantle discontinuity structure beneath eastern North America. J. Geophys. Res. 110 (B5), 2100. doi:10.1029/2001JB000190.

Li, X., Kind, R., Yuan, X., Wölbern, I., Hanka, W., 2004. Rejuvenation of the lithosphere by the Hawaiian plume. Nature 427, 827–829.

Li, C., van der Hilst, R.D., Nafi Toksöz, M., 2006a. Constraining *P*-wave velocity variations in the upper mantle beneath Southeast Asia. Phys. Earth Planet. Inter. 154, 180–195.

Li, S., Mooney, W.D., Fan, J., 2006b. Crustal structure of mainland China from deep seismic sounding data. Tectonophysics 420, 239–252.

Li, X., Yuan, X., Kind, R., 2007. The lithosphere–asthenosphere boundary beneath the western United States. Geophys. J. Int. 170, 700–710.

Liu, H.F., Liang, H.S., Li, X.Q., Yin, J.G., Zhu, D.F., Liu, L.Q., 2000. The coupling mechanisms of Mesozoic–Cenozoic rift basins and extensional mountain system in Eastern China. Earth Sci. Geosci. 7, 477–486 (in Chinese).

Liu, M., Yang, Y., Shen, Z., Wang, S., Wang, M, Wan, Y., 2007. Active tectonics and intracontinental earthquakes in China: the kinematics and geodynamics. In: Stein, S., Mazzotti, S. (Eds.), Continental intraplate earthquakes: science, hazard, and policy issues: Geological Society of America Special Paper, vol. 425, pp. 299–318.

Ma, X.Y., 1989. Lithospheric Dynamics Map of China and Adjacent Seas (1:4,000,000) and Explanatory Notes, Geological Publishing House, Beijing, China.

Meng, Q.R., 2003. What drove late Mesozoic extension of the northern China–Mongolia tract? Tectonophysics 369, 155–174.

Menzies, M.A., Fan, W.M., Zhang, M., 1993. Palaeozoic and Cenozoic lithoprobes and the loss of N120 km of Archaean lithosphere, Sino-Korean craton, China. In: Prichard, H.M., Alabaster, T., Harris, N.B.W., Neary, C.R. (Eds.), Magmatic processes and plate tectonics: Geol. Soc. Spel. Pub., vol. 76, pp. 71–78.

Menzies, M.A., Xu, Y.G., 1998. Geodynamics of the North China Craton. In: Flower, M., Chung, S.L., Lo, C.H., Lee, T.Y. (Eds.), Mantle dynamics and plate interactions in East Asia: Am. Geophys. Union Geodyn. Ser., vol. 27, pp. 155–165.

Menzies, M.A., Xu, Y.G., Zhang, H.F., Fan, W.M., 2007. Integration of geology, geophysics and geochemistry: a key to understanding the North China Craton. Lithos 96, 1–21.

Pei, S., Zhao, J., Sun, Y., Xu, Z., Wang, S., Liu, H., et al., 2007. Upper mantle seismic velocities and anisotropy in China determined through Pn and Sn tomography. J. Geophys. Res. 112, B05312. doi:10.1029/2006JB004409.

Ren, J., Tamaki, K., Li, S., et al., 2002. Late Mesozoic and Cenozoic rifting and its dynamic setting in Eastern China and adjacent areas. Tectonophysics 344, 175–205.

Savage, B., Silver, P.G., 2008. Evidence for a compositional boundary within the lithospheric mantle beneath the Kalahari craton from S receiver functions. Earth Planet. Sci. Lett. 272, 600–609.

Shomali, Z.H., Roberts, R.G., Pedersen, L.B., TOR Working Group, 2006. Lithospheric structure of the Tornquist Zone resolved by nonlinear P and S teleseismic tomography along the TOR array. Tectonophysics 416, 133–149.

Simons, F.J., Zielhuis, A., van der Hilst, R.D., 1999. The deep structure of the Australian continent from surface wave tomography. Lithos 48, 17–43.

Sun, Y., Toksöz, M.N., 2006. Crustal structure of China and surrounding regions from P wave traveltime tomography. J. Geophys. Res. 111, B03310. doi:10.1029/2005JB003962.

Sun, Y., Toksöz, M.N., Pei, S., Morgan, F.D., 2008. The layered shear-wave velocity structure of the crust and uppermost mantle in China. Bull. Seismol. Soc. Am. 98 (2) 746–755.

Tang, Y.J., Zhang, H.F., Ying, J.F., Zhang, J., Liu, X.M., 2008. Refertilization of ancient lithospheric mantle beneath the central North China Craton: evidence from petrology and geochemistry of peridotite xenoliths. Lithos 101, 435–452.

Tian, Y., Zhao, D., Sun, R., Teng, J., 2009. Seismic imaging of the crust and upper mantle beneath the North China Craton. Phys. Earth Planet. Int. 172, 169–182.
Wang, H., Mo, X., 1995. An outline of tectonic evolution of China. Episodes 18, 6–16.
Wang, J.Y., Huang, S.P., Chen, M.X., 1996. Terrestrial heat flux map (in Chinese). In: Yuan, X.C. (Ed.), Geophysical Atlas in China. Geophysical Publishing House, Beijing, p. 102.
Wang, Y.J., Fan, W.M., Zhang, H.F., Peng, T.P., 2006. Early Cretaceous gabbroic rocks from the Taihang Mountains: implications for a paleosubduction-related lithospheric mantle beneath the central North China Craton. Lithos 86, 281–302.
Windley, B., Alexeiev, D., Xiao, W., Kröner, A., Badarch, G., 2007. Tectonic models for accretion of the Central Asian Orogenic Belt. J. Geol. Soc. 164, 31–47.
Wittlinger, G., Farra, V., Vergne, J., 2004. Lithospheric and upper mantle stratifications beneath Tibet: new insights from Sp conversions. Geophys. Res. Lett. 31, L19615. doi:10.1029/2004GL020955.
Wittlinger, G., Farra, V., 2007. Converted waves reveal a thick and layered tectosphere beneath the Kalahari super-craton. Earth Planet. Sci. Lett. 254, 404–415.
Wu, F.Y., Ge, W.C., Sun, D.Y., 2003. Discussion on lithospheric thinning in eastern China. Earth Sci. Front. 10, 51–60 (in Chinese).
Wu, F.Y., Lin, J.Q., Wilde, S.A., Zhang, X.O., Yang, J.-H., 2005. Nature and significance of the Early Cretaceous giant igneous event in eastern China. Eartn Planet Sci. Lett. 233, 103–119.
Xu, Y.G., 2001. Thermotectonic destruction of the Archean lithospheric keel beneath eastern China: evidence, timing, and mechanism. Phys. Chem. Earth A 26, 747–757.
Xu, Y.G., 2007. Diachronous lithospheric thinning of the North China Craton and formation of the Daxin'anling–Taihangshan gravity lineament. Lithos 96, 281–298.
Xu, Y.-G., Huang, X.L., Ma, J.L., Wang, Y.B., Iizuka, Y., Xu, J.F., Wang, Q., Wu, X.Y., 2004. Crustal–mantle interaction during the thermo-tectonic reactivation of the North China Craton: SHRIMP zircon U–Pb age, petrology and geochemistry of Mesozoic plutons in western Shandong. Contrib. Minera. Petrol. 147, 750–767.
Yin, A., Nie, S.Y., 1993. An indentation model for the North and South China collision and the development of the Tan–Lu and Honam Fault Systems, eastern Asia. Tectonics 12, 801–813.
Zhai, M.-G., Liu, W.J., 2003. Paleoproterozoic tectonic history of the North China craton: a review. Precambrian Res. 122, 183–199.
Zhang, K.J., 1997. North and South China collision along the eastern and southern North China margins. Tectonophysics 270, 145–156.
Zhang, H.F., 2005. Transformation of lithospheric mantle through peridotite–melt reaction: a case of Sino-Korean craton. Earth Planet. Sci. Lett. 237, 768–780.
Zhang, Y.Q., Mercier, J.L., Vergély, P., 1998. Extension in the graben systems around the Ordos (China), and its contribution to the extrusion tectonics of south China with respect to Gobi-Mongolia. Tectonophysics 285, 41–75.
Zhang, Y.Q., Ma, Y.S., Yang, N., Shi, W., Dong, S., 2003. Cenozoic extensional stress evolution in North China. J. Geodyn. 36, 591–613.
Zhao, G.C., Wilde, S.A., Cawood, P.A., Sun, M., 2001. Archean blocks and their boundaries in the North China Craton: lithological, geochemical, structural and P–T path constraints and tectonic evolution. Precambrian Res. 107, 45–73.
Zhao, L., Zheng, T., Lü, G., 2008. Insight into craton evolution: constraints from shear wave splitting in the North China Craton. Phys. Earth Planet. Int. 168, 153–162.
Zheng, J., O'Reilly, S.Y., Griffin, W.L., Lu, F., Zhang, M., 1998. Nature and evolution of Cenozoic lithospheric mantle beneath Shandong peninsula, Sino–Korean craton. Int. Geol. Rev. 40, 471–499.
Zheng, T., Chen, L., Zhao, L., Xu, W.W., Zhu, R., 2006. Crust–mantle structure difference across the gravity gradient zone in North China Craton: seismic image of the thinned continental crust. Phys. Earth Planet. Int. 159, 43–58.
Zheng, T., Zhao, L., Zhu, R.X., 2009. New evidence from seismic imaging for subduction during assembly of the North China Craton. Geology 37, 395–398.
Zhu, J., Cao, J., Cai, X., Yan, Z., Cao, X., 2002. High resolution surface wave tomography in east Asia and west Pacific marginal seas. Chin. J. Geophys. 45 (5), 646–664 (in Chinese with English abstract).
Zielhuis, A., Nolet, G., 1994. Deep seismic expression of an ancient plate boundary in Europe. Science 265, 79–81.
Zielhuis, A., van der Hilst, R.D., 1996. Upper-mantle shear velocity beneath eastern Australia from inversion of waveforms from SKIPPY portable arrays. Geophys. J. Int. 127, 1–16.
Zorin, Y.A., 1999. Geodynamics of the western part of the Mongolia–Okhotsk collisional belt, Trans–Baikal region (Russia) and Mongolia. Tectonophysics 306, 33–56.